RESEARCH ARTICLE

High-Energy–Density Fiber Supercapacitors Based on Transition Metal Oxide Nanoribbon Yarns for Comprehensive Wearable Electronics

Junseong Ahn[1] · Suchithra Padmajan Sasikala[2,3] · Yongrok Jeong[6] · Jin Goo Kim[2,3] · Ji-Hwan Ha[4,5] · Soon Hyoung Hwang[5] · Sohee Jeon[5] · Junhyuk Choi[5] · Byung-Ho Kang[4,5] · Jihyeon Ahn[4] · Jun-Ho Jeong[5] · Sang Ouk Kim[2,3] · Inkyu Park[4]

Abstract

Fiber supercapacitors (FSs) based on transition metal oxides (TMOs) have garnered considerable attention as energy storage solutions for wearable electronics owing to their exceptional characteristics, including superior comfortability and low weights. These materials are known to exhibit high energy densities, high specific capacitances, and fast redox reactions. However, current fabrication methods for these structures primarily rely on chemical deposition, often resulting in undesirable material structures and necessitating the use of additives, which can degrade the electrochemical performance of such structures. Herein, physically deposited TMO nanoribbon yarns generated via delamination engineering of nanopatterned TMO/metal/TMO trilayer arrays are proposed as potential high-performance FSs. To prepare these arrays, the target materials were initially deposited using a nanoline mold, and subsequently, the nanoribbon was suspended through selective plasma etching to obtain the desired twisted yarn structures. Because of the direct formation of TMOs on Ni electrodes, a high energy/power density and excellent electrochemical stability were achieved in asymmetric FS devices incorporating $CoNi_xO_y$ nanoribbon yarns and graphene fibers. Furthermore, a triboelectric nanogenerator, pressure sensor, and flexible light-emitting diode were synergistically combined with the FS. The integration of wearable electronic components, encompassing energy harvesting, energy storage, and powering sensing/display devices, is promising for the development of future smart textiles.

Junseong Ahn, Suchithra Padmajan Sasikala, Yongrok Jeong, Jun-Ho Jeong, Sang Ouk Kim and Inkyu Park have contributed equally to the work.

✉ Jun-Ho Jeong
jhjeong@kimm.re.kr

✉ Sang Ouk Kim
sangouk@kaist.ac.kr

✉ Inkyu Park
inkyu@kaist.ac.kr

1   Department of Electro-Mechanical Systems Engineering, Korea University, Sejong 30019, Republic of Korea

2   Department of Materials Science and Engineering, Korea Advanced Institute of Science and Technology (KAIST), Daejeon 34141, Republic of Korea

3   National Creative Research Initiative Center for Multi-Dimensional Directed Nanoscale Assembly, Korea Advanced Institute of Science and Technology (KAIST), Daejeon 34141, Republic of Korea

4   Department of Mechanical Engineering, Korea Advanced Institute of Science and Technology (KAIST), Daejeon 34141, Republic of Korea

5   Department of Nano Manufacturing Technology, Korea Institute of Machinery and Materials (KIMM), Daejeon 34103, Republic of Korea

6   Radioisotope Research Division, Korea Atomic Energy Research Institute (KAERI), Daejeon 34057, Republic of Korea

1 Introduction

Research on fiber supercapacitors (FSs) has gained traction in the realm of wearable electronics owing to their potential as efficient energy storage solutions in various domains, including healthcare, environmental monitoring, and military applications [1–10]. Unlike conventional rigid and bulky cell or film-type supercapacitors, FSs offer exceptional adaptability for integration into textiles and other nonplanar geometries. This advantage stems from their inherent softness, mechanical flexibility, thin and lightweight characteristics, as well as their quick charge–discharge capabilities and long lifecycles [11–15].

FSs typically consist of an electric double-layer capacitor (EDLC) material, such as carbon nanotube (CNT) yarns or graphene fibers (GFs), known for their excellent electrical conductivities across extended voltage ranges [15–19]. However, their limited electrochemical activities and low-energy densities pose a challenge to their direct application in advanced energy storage devices [20]. To enhance electrochemical performances, the incorporation of pseudocapacitive materials becomes imperative [21].

Transition metal oxides (TMOs) play a pivotal role as intercalation pseudocapacitors owing to their high theoretical specific capacity, structural versatility, and low costs [22–26]. However, the intrinsically low electronic conductivity of most TMOs limits their energy densities, and the volume expansion during cycling further affects their cycle stability. Direct growth of TMOs on a conductive substrate is considered an efficient strategy to overcome these limitations. In addition to the mechanical reinforcement, such conductive substrates accelerate the transport kinetics and reduce the internal resistance between the active TMO material and the current collector. TMOs compounded with conductive substrates such as graphene, CNTs, activated carbon, and MXenes, exhibit excellent catalytic activities and long lifecycles [27–29]. Nevertheless, the existing synthetic methods for TMOs, such as solution phase chemical precipitation and/or hydrothermal treatment, are not optimized for fiber morphology [30–32].

In this study, we developed a straightforward synthesis method for scalable and reliable production of TMO yarns that can be readily used as FSs without requiring additives or current collectors. As shown in Fig. 1, dimension-controlled pseudocapacitive TMO yarns with high electrochemical activities and rate capabilities are fabricated by twisting the TMO/metal/TMO trilayer nanoribbon arrays, which are formed using industrially adaptable nanoimprinting lithography (NIL) and electron-beam (e-beam) evaporation procedures. Specifically, a sandwiched metal layer included in our optimized unique trilayer nanoribbon structure enhances the mechanical robustness and electronic conductivity of the structure by forming electron transfer pathways, and the ultrathin (~ 150 nm) porous structure of the top and bottom
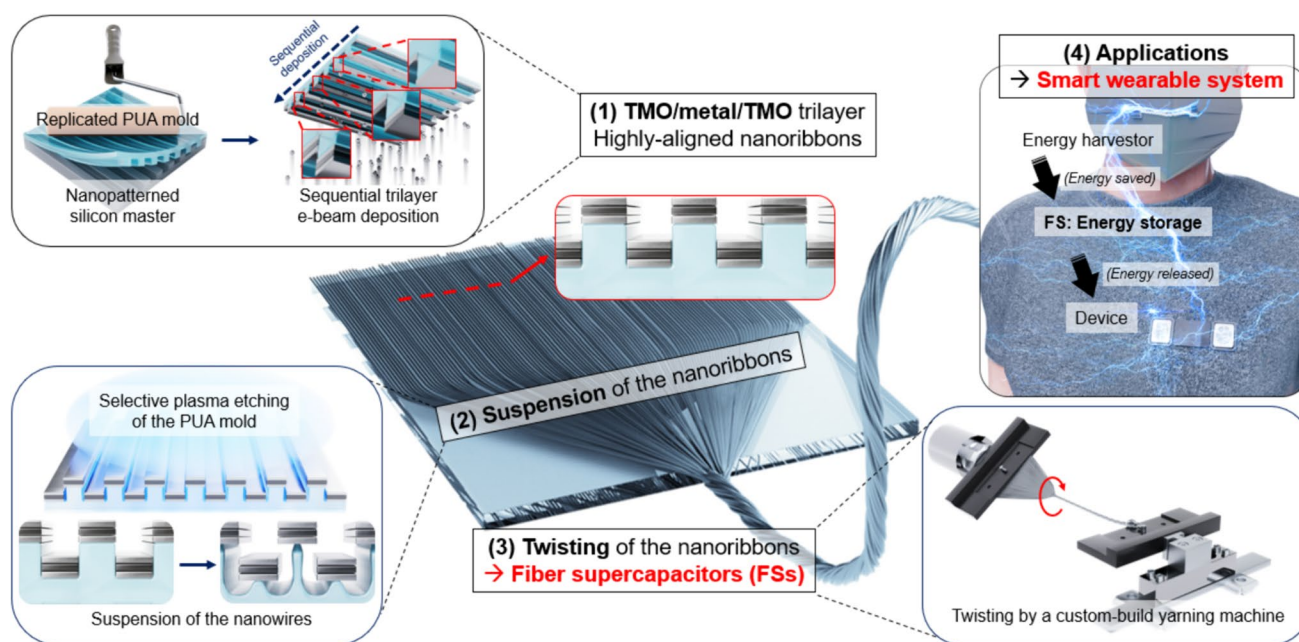
Fig. 1 Overall concept of the developed FS. Through the rational combination of NIL and delamination engineering, various TMO/metal/TMO trilayer nanoribbon yarns were developed for use in high-performance FSs. Various wearable devices, including a TENG, pressure sensor, and a flexible LED are integrated with the nanoribbon yarn FS to demonstrate various types of comprehensive wearable electronic systems ranging from energy harvesting and energy storage to power devices

TMO layers provides large electrolyte–active material contact areas and short ionic diffusion paths.

To demonstrate the versatility of our developed synthetic method, different TMO-based yarns, such as NiOx@Ni (NO), MnOx@Ni (MO), and CoNixOy@Ni (CNO), were fabricated, which exhibited high electrochemical activities and long electrochemical stability when employed as FSs. Notably, the symmetric FS (sFS), based on two parallel CNO yarns, demonstrated an exceptionally high specific capacitance of 365.3 F/cm^3, and the asymmetric FS (aFS) device, which was prepared using a GF and CNO yarn as the negative and positive electrodes, respectively, displayed exceptional energy (91.75 mWh/cm^3) and power densities (648.3 mW/cm^3). In addition, a range of wearable electronic systems integrated with our FSs were demonstrated owing to the ability of these FSs to retain their specific capacitance even after several mechanical deformation steps and prolonged electrochemical cycles (10000 cycles). In each system, a triboelectric nanogenerator (TENG) was used to charge the FS, which was then employed to power a pressure sensor and flexible light-emitting diodes (LEDs) for incorporation into wearable devices. To the best of our knowledge, this paper reports the highest capacitance and energy density achieved in FSs to date and demonstrates comprehensive wearable electronic systems, integrating harvesting, storage, and powering functional devices, for the first time. The ability to fabricate a high-performance FS, store mechanical energy from human breathing into the FS, and utilize this FS to power various electronic devices exemplifies the great potential of the developed technology to advance the field of wearable energy storage and power solutions.

2 Results

2.1 Fabrication of Trilayer Nanoribbon Yarns for FSs

To obtain high-performance wearable FSs, a fabrication approach involving TMO nanoribbon yarns and precise delamination engineering was developed (Figs. 1 and S1). This process consists of three key steps; first, to create a sandwich-like TMO–Ni–TMO trilayer nanoribbon structure, TMO, Ni, and TMO layers were sequentially deposited on a nanoimprinted polymeric mold using an e-beam evaporator. Second, the formed thin nanoribbon array was delaminated without fracture by minimizing the adhesion between the mold and deposited trilayer; specifically, the nanopatterned polymer mold was selectively and gradually etched by oxygen plasma treatment (as shown in Fig. S2) [33, 34], which suppressed the adhesion and enabled facile delamination of the trilayer nanoribbon array. Lastly, the delaminated trilayer nanoribbon array was gently twisted into a one-dimensional

(1D) yarn using a yarning machine for application in high-performance wearable devices.

In the aforementioned process, various combinations of TMOs and metals compatible with the e-beam evaporator can be used to fabricate nanoribbon yarns. In this study, Ni was selected to form the central layer owing to its low cost, high electrochemical stability, and good electrical conductivity. NiOx, MnOx, and CoNixOy were selected to form the top and bottom TMO layers because of their high energy densities and excellent specific capacitances [35, 36]. The successful fabrication of the desired materials was confirmed using transmission electron microscopy (TEM) and energy-dispersive spectroscopy (EDS); the obtained side-view images of the nanopatterned molds are presented in Fig. 2a. Each TMO (NiOx-, MnOx-, and CoNixOy-)-based trilayer nanoribbon was initially deposited with a middle layer of Ni (thickness: 150–200 nm), and top and bottom TMO (~100 nm) layers, to create a sandwich structure. Subsequently, the delaminated trilayer nanoribbon array was twisted into a yarn structure (Fig. 2b), whose formation was confirmed through scanning electron microscopy (SEM) and EDS observations. Although the yarn morphology varied owing to the different intrinsic properties of each material and the residual stress during deposition, all the nanoribbon arrays were successfully transformed into yarn structures with lengths of few centimeters and an approximate diameter of 200 μm (Fig. S3). Remarkably, despite the high inherent brittleness of the bulk TMOs, the nanoscale thicknesses of the individual nanoribbons drastically reduced their flexural rigidity, thus imparting softness to the nanoribbon structures. As a result, highly flexible and deformable 1D yarns composed of the nanoribbon arrays were successfully produced [37].

Subsequently, the material compositions of the obtained yarns were assessed using X-ray photoelectron spectroscopy (XPS), and the corresponding profiles are depicted in Fig. 2c. The Ni $2p_{3/2}$ peak was deconvoluted into Ni^0 (852.5 eV), Ni^{2+} (854.4 eV), and Ni^{3+} (856.0 eV) peaks, whereas the Mn $2p_{3/2}$ peak was deconvoluted into Mn^0 (639.0 eV), Mn^{1+} (642.6 eV), Mn^{2+} (640.5 eV), and Mn^{3+} (641.5 eV) peaks. Additionally, the Co $2p_{3/2}$ peak was deconvoluted into Co^0 (777.9 eV), Co^{2+} (780.4 eV), Co^{3+} (781.3 eV), and satellite Co^{3+} (787.6 eV) peaks [38–40]. These results indicate that each TMO nanoribbon yarn comprised various NiO$_x$ (NiO and Ni$_2$O$_3$), MnO$_x$ (MnO, MnO$_2$, and Mn$_2$O$_3$), and CoO$_x$ (CoO and Co$_2$O$_3$) species. The binding energies of all the elements were calibrated to the adventitious carbon peak (284.8 eV), and spectral fitting was performed using the least-squares method to minimize any bias arising from manual fitting. In this study, the choice of NiO$_x$ was based on its high capacitance and rate capability; MnO$_x$ was selected owing to its high capacitance, natural abundance, and relatively low cost [36]; the CoNi$_x$O$_y$ component
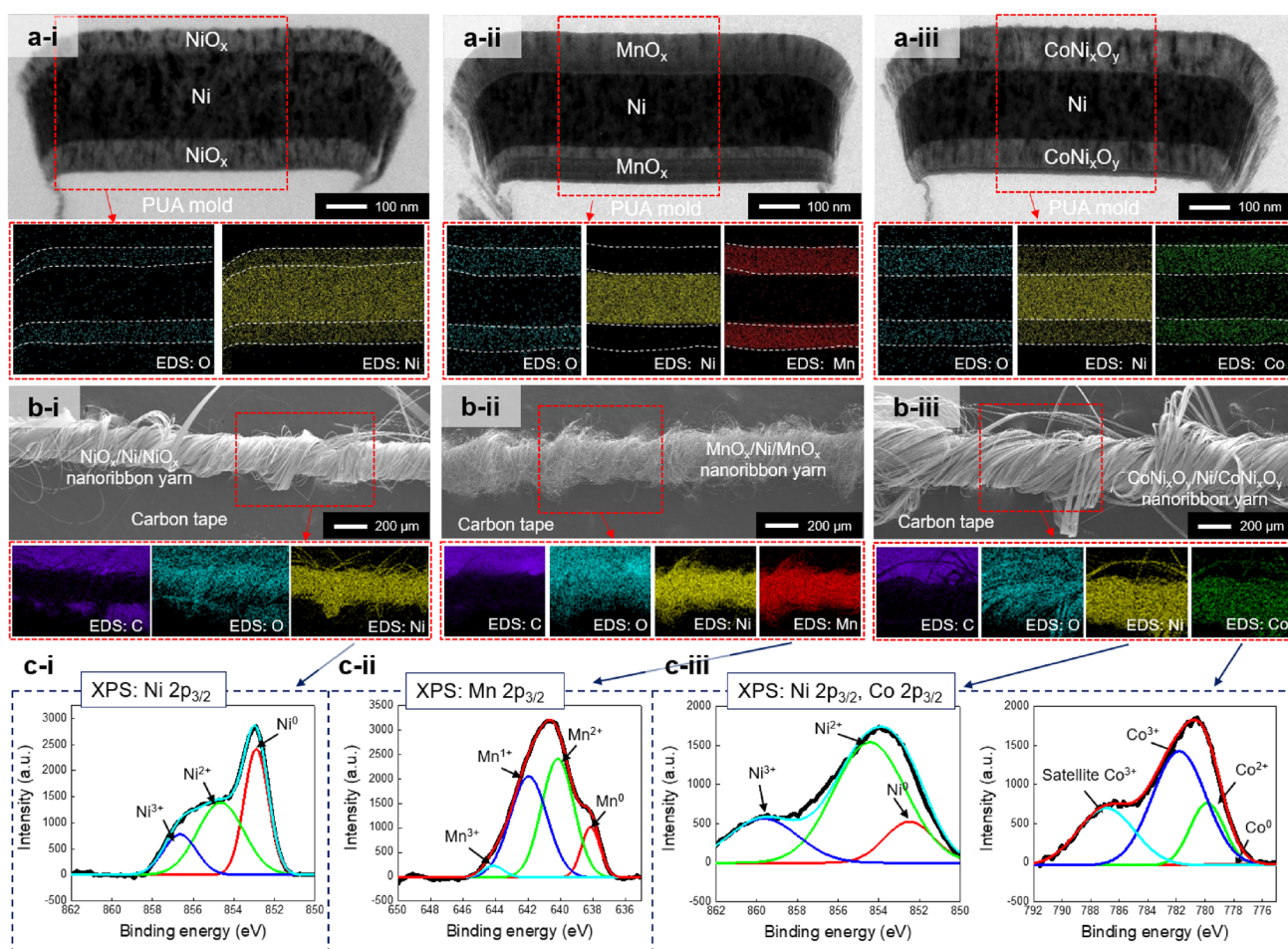
Fig. 2 Material and structural analyses of the NO, MO, and CNO nanoribbon yarns. TEM and EDS images of the individual (**a-i**) NO, (**a-ii**) MO, and (**a-iii**) CNO nanoribbons, demonstrating their TMO/metal/TMO sandwich structures. SEM and EDS images of the final (**b-i**) NO, (**b-ii**) MO, and (**b-iii**) CNO nanoribbon yarns. XPS profiles of the (**c-i**) NO, (**c-ii**) MO, and (**c-iii**) CNO nanoribbon yarns, demonstrating their material compositions

was selected as a representative ternary TMO because of its high specific capacitance and electrical conductivity, which were superior to those of binary TMOs; these properties of CoNi$_x$O$_y$, which is an excellent pseudocapacitive material, are attributed to its multiple oxidation states and metal cations [35, 41].

2.2 Electrochemical Performances of the TMO Nanoribbon Yarns

A wearable sFS device was fabricated by placing two similar TMO yarns in a parallel arrangement on a flexible substrate (e.g., a polyethylene terephthalate (PET) film or fabric). A polyvinyl alcohol/potassium hydroxide (PVA/KOH) electrolyte, which also served as a separator between the electrodes, was deposited on top of the yarns (Fig. S4). The capacitive performance of each sFS-based assembled yarn was then evaluated by cyclic voltammetry (CV) and galvanostatic

charge–discharge (GCD) measurements in the potential range of 0–0.45 V while varying the scan rates and current densities. As shown in Fig. 3a, c, e, the CV plots of the NO, MO, and CNO sFSs deviate from the typical rectangular shapes owing to the occurrence of Faradaic processes at the electrode–electrolyte interfaces. These CV profiles are retained even at a high scan rate of 100 mV/s, illustrating the remarkably high-rate performances and swift charge transport properties of these materials. The anodic and cathodic redox peaks consistently shift toward the higher and lower potentials, respectively, indicating the excellent reversibility of the redox reactions. The swift increase in the current density at high voltages for NO indicates a synergistic combination of double-layer capacitance and pseudocapacitance behaviors, typical of layered TMOs. The pseudocapacitive contribution due to fast surface redox reactions and ion intercalation becomes significant at high potentials, resulting in a rapid increase in current. To compare the capacitance and
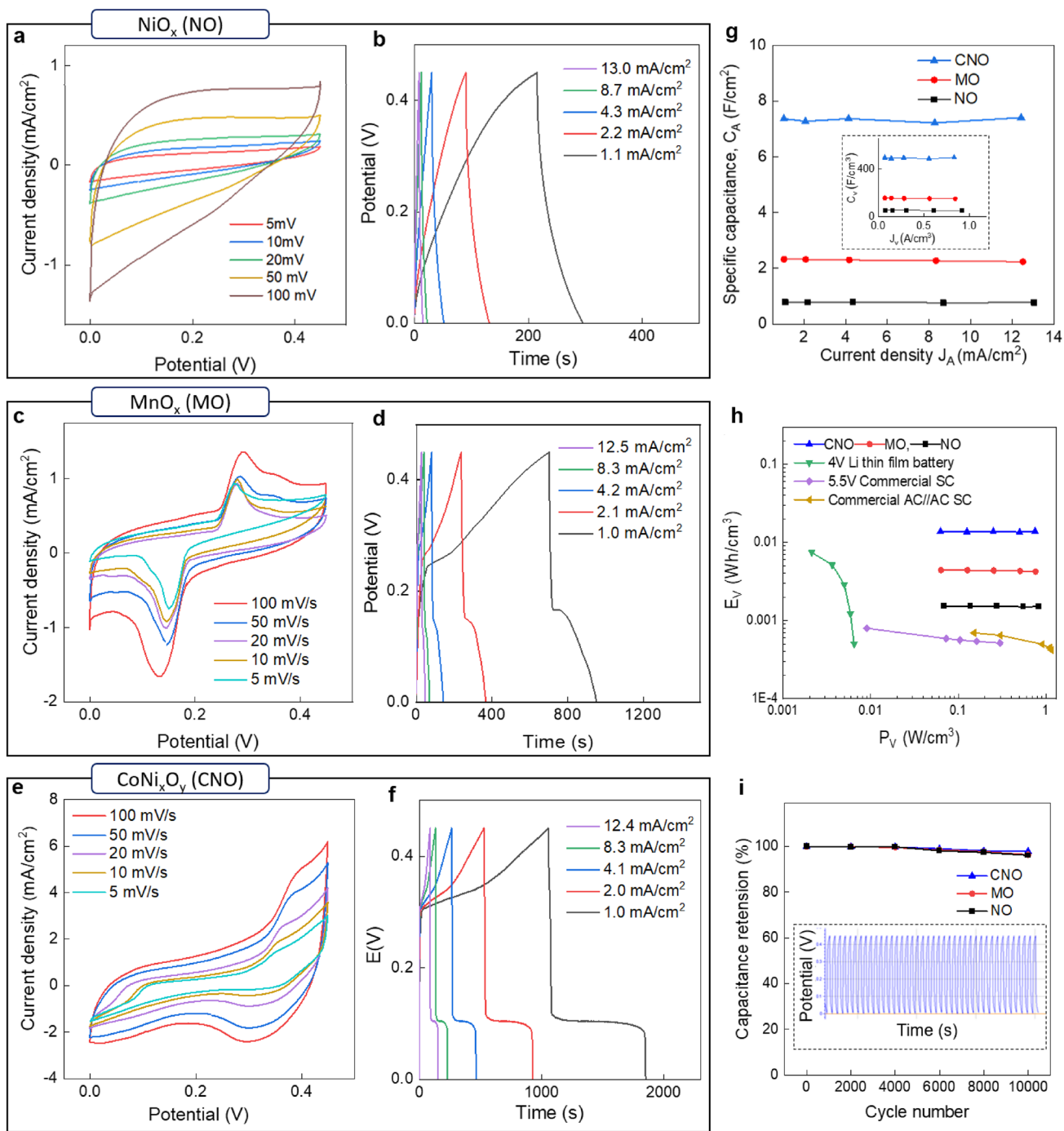
Fig. 3 Electrochemical performances of the sFS devices. **a, c, e** CV plots at various scan rates, and **b, d, f** GCD plots at various current densities for the (**a, b**) NO, (**c, d**) MO, and (**e, f**) CNO yarn-based sFSs. The minor variation in the current density is due to the difference in the electrode area. **g** Arial capacitances of the sFSs at increasing current densities. The corresponding volumetric capacitances are given in the inset. **h** Comparison of the energy densities of the sFSs with a 4 V/500 µAh thin-film lithium battery and commercially available supercapacitors. **i** Capacitance retentions of the sFSs. The GCD profiles of the CNO sFS recorded over several cycles are shown in the inset

energy density variations of the three tested CNO yarns, the voltage window was set as 0–0.45 V (unless stated otherwise). The GCD plots for the MO and CNO sFSs at different

current densities indicate that their discharge behaviors are characterized by a rapid voltage drop followed by the emergence of a plateau (Fig. 3b, d, f). This behavior can

be attributed to the nanostructured porous structures of the electrode materials, which exhibit battery-like charge storage behaviors while generating a substantial electrochemical double-layer capacitance [42–44]. As a result, an initial rapid voltage drop occurs along with the discharge of the double-layer capacitance, which is followed by the emergence of a phase transformation plateau. This plateau is characterized by a prolonged discharge period, which enables diffusion of the reactants into the inner pores, resulting in a high specific capacitance. Notably, the cathodic redox peaks observed in the CV plots of the CNO sFSs disappear from their discharge profile. As CV involves dynamic and continuous potential scanning to drive oxidation and reduction processes at a constant scan rate, it allows the observation of electrochemical processes over a broad range of potentials. Conversely, in the discharge plot, the observed potential response naturally originates from the system delivering a fixed current. The rapid voltage drop at higher potentials and the long plateau at lower potentials in the discharge profile of the CNO sFS are indicative of the differences in the kinetics of ionic diffusion, charge transfer, and electrochemical reactions at different discharge rates. These surface modifications that occur during cycling, leading to changes in the electrochemical behavior of this CNO sFS, are typical of battery-like materials [45].

The integrated area of the CV plot at a particular scan rate and the discharge time of the GCD plot correspond to the specific capacitance of the sFS at a particular current density. Accordingly, the specific capacitances of the developed sFSs decrease in the order of CNO > MO > NO. Owing to the extremely low mass loadings, which are considerably lower than those bulk or film-type supercapacitors, FSs tend to exhibit unusually high gravimetric capacitance values, which may not represent their meaningful capacities in real practice [44]. Therefore, to assess the viability of an FS, its areal capacitance values are measured. To account for the variation in the thickness of the FSs due to the use of different yarns, we also calculated the volumetric capacitance, following an analysis of the average diameter of the yarns using SEM (Fig. 2a, b). As shown in Fig. 3g, the areal and volumetric capacitance values of the CNO sFS reach 7.36 F/cm^2 and 493.34 F/cm^3 at current densities of 1.03 mA/cm^2 and 69.37 mA/cm^3, respectively. The corresponding areal and volumetric specific capacity values are 3.31 C/cm^2 and 222.02 C/cm^3, respectively.

Notably, the specific capacitance of the CNO sFS is a magnitude higher than those of the previously reported high-performing biscrolled MnO_2/CNT yarns (0.88 F/cm^2, 154.7 F/cm^3) [46], poly(3,4-ethylenedioxythiophene) (PEDOT)/reduced graphene oxide (rGO) core–shell fibers (0.83 F/cm^2, 263.1 F/cm^3) [22], rGO/CNT composite fibers (0.17 F/cm^2, 158 F/cm^3) [1], and PEDOT/CNT yarns (0.073 F/cm^2, 179 F/cm^3) [46] (Table S1). Similarly, the MO

and NO sFSs exhibit high areal specific capacitances of 2.32 and 0.78 F/cm^2 at current densities of 1.04 and 1.08 mA/cm^2, respectively; their corresponding volumetric capacitances are 156.6 and 54.7 F/cm^3 at 70.3 and 76.2 mA/cm^3, respectively. In addition, the areal and volumetric specific capacities of the MO sFSs are 1.04 C/cm^2 and 70.47 C/cm^3, respectively, and those of the NO sFSs are 0.35 C/cm^2 and 24.64 C/cm^3, respectively. The specific capacitances of the Ni–Co binary oxides in the CNO sFS are higher than those of the monometallic NO and MO electrodes owing to the synergetic effect between the Ni and Co species, which can afford a richer variety of redox reactions than those taking place in monometallic oxide materials.

The mechanism of charge storage can be distinguished using the power-law equation, which expresses the dependence of the current (j) response on the sweep rate (υ) as $j = aυ^b$, where a and b are variables. In this study, we set b = 0.5 and 1 for diffusion-controlled (solid-state ionic) and nondiffusion-controlled (capacitive) charge storage, respectively. As shown in Fig. S5, the b values for the CNO, MO, and NO yarns are 0.61, 0.66, and 0.75, respectively, which indicate that both mechanisms exist simultaneously in our yarns. However, the semi-infinite diffusion process, which is typical for intercalating battery materials, dominates in the CNO and MO yarns, whereas the resulting current in NO is ascribed to a hybrid diffusion-controlled and capacitive mechanism.

Electrochemical impedance spectroscopy (EIS) tests were conducted to assess the electrochemical mass transfer resistance caused by electrolyte transport within the electrode pores (Fig. S6a). The small semicircle in the high-frequency segment can be attributed to the charge transfer resistance, while the linear slope in the low-frequency segment is indicative of the mass transfer resistance. The internal resistance, which encompasses various factors, including the inherent resistance of the active materials, ionic resistance of the electrolyte, and resistance at the interface between the active material and current collector, can be determined from the intercept of the plot with the real axis in the high-frequency domain [47]. Evidently, the prepared sFSs display a negligible real-axis intercept (< 10.0 Ω), which highlights their low internal resistances. Notably, the internal resistance of the CNO sFS (~ 3.58 Ω) is lower than that of the MO (~ 5.08 Ω) and NO (7.04 Ω) sFSs; thus, the electrical conductivity of the CNO sFS is superior to those of the other two fabricated sFSs, and consequently, the CNO sFS exhibits the highest specific capacitance among all the sFSs prepared in this study (Fig. S6b). In addition, the calculated areal energy densities (E_A) for the CNO, MO, and NO sFSs are 0.20, 0.06, and 0.02 mWh/cm^2 for power densities (P_A) in the range of 0.93–0.97 mW/cm^2. The corresponding volumetric energy densities (E_V) for the CNO, MO, and NO sFSs are 0.138, 0.004, and 0.002 Wh/cm^3,

respectively. The remarkable performances of these sFSs are illustrated through a Ragone plot (Fig. 3h), which also compares their energy densities to those of a commercially available 4 V/500 µAh thin-film lithium battery (<0.01 Wh/cm^3), 5.5 V conventional supercapacitor (<0.001 Wh/cm^3), and commercial alternating-current supercapacitor (<0.0001 Wh/cm^3) (see Table S1) [16, 48, 49].

To assess the cycling stability of the prepared systems, GCD tests were conducted over 10,000 cycles at current densities in the range of 12–13 mA/cm^2. As illustrated in Fig. 3i, the three prepared sFSs demonstrate exceptional cycling stability and retain more than 97.3% of their initial capacitances, thus ultimately indicating high reversibility. These remarkable capacitance retention characteristics, which are superior to those of other previously reported battery-like/pseudocapacitive materials, can be ascribed to the binder-free nanoporous structures of the sFSs as well as the minimal degrees of metal oxide agglomeration in the present yarns. Overall, these characteristics collectively enhance the Faradaic processes, particularly the efficient transport and diffusion of ions and electrons between the active metal oxide material and electrolyte. This synergistic combination of a high specific capacitance, robust rate capability, and long cycling life indicate the potential of these NO, MO, and CNO yarns as compelling candidates for end-use wearable FSs.

To expand the potential window of these yarn-based electrodes further for practical applications, a hybrid aFS was assembled using the prepared CNO yarn as the positive electrode, GFs or MXene fibers (MFs) as the negative electrode, and PVA/KOH gel as the electrolyte (Fig. 4a). Evidently, the combination of a large-capacity battery-type CNO and an EDLC-type GF/MF successfully improves the energy density while retaining a long cycle life, which is typical of an electrochemical capacitor. The electrochemical properties of the GF/CNO (G-CNO) and MF-CNO (M-CNO) aFSs were evaluated by CV and GCD measurements over a broadened operational potential window of 0–1.5 V (Figs. 4b, c, and S7a). This voltage window was chosen to maximize the energy density of the supercapacitor while avoiding the decomposition of the aqueous electrolyte, which typically occurs at voltages >1.5 V. A comparison of the CV plots of the aFSs with those of the GF, MF, and CNO yarn FSs, obtained at a scan rate of 20 mV/s (Fig. 4b), reveals the capacitive performance of the G-CNO aFS is superior to that of the M-CNO aFS. In addition, the capacitive performance of the hybrid aFS incorporating the CNO electrode and PVA/KOH gel electrolyte surpasses that of an aFS comprising a PVA/Na$_2$SO$_4$ gel electrolyte and the CNO electrode. Consequently, the PVA/KOH gel electrolyte was selected for further aFS characterizations. Upon varying the scan rate from 10 to 100 mV/s, no obvious distortion in the CV plots is observed for the G-CNO aFS, indicating its high stability

(Fig. S7a). Moreover, the efficient adsorption and desorption of the electrolyte ions at the fiber electrode surfaces are implied by the linear correlation between the discharge current density and scan rate (Fig. S7b). Similarly, the GCD plots of the G-CNO and M-CNO aFSs are measured in the voltage range of 0–1.5 V, and a stable nonlinear behavior is verified at current densities ranging from 1.0 to 5.3 mA/cm^2 (Figs. 4c and S8). In addition, the calculated specific capacitances of the G-CNO and M-CNO aFSs reach 214.19 and 166.35 F/cm^3 at current densities of 0.17 and 0.19 A/cm^3, respectively; the corresponding areal capacitances are 2.93 and 2.08 A/cm^2 for current densities of 2.2 and 2.4 mA/cm^2, respectively. Figures S9a and S9b show the specific capacitances of the G-CNO and M-CNO aFSs as functions of the current density. The maximum E_A values of the G-CNO and M-CNO aFSs in the voltage range of 0–1.5 V are 1.04 and 0.61 mWh/cm^2 (76.15 and 48.57 mWh/cm^3), respectively (Figs. S9c and S9d). This remarkable energy density indicates the superiority of this G-CNO aFS over all the aFS systems reported to date (Table S2). Furthermore, as presented in Fig. 4d, e, the working voltage range can be further extended to 3 and 6 V by connecting two and four aFSs in series. The corresponding specific capacitances and voltage ranges of both the series-connected aFSs and CNO sFS are presented in Fig. 4f. The CNO sFS exhibits a higher specific capacitance than does the corresponding aFSs; however, the maximum voltage range of the former falls below 2.0 V, which has a detrimental effect on the resulting energy density. In contrast, the G-CNO and M-CNO aFSs exhibit comparable specific capacitances, an extremely high potential range of 6 V is achieved when four of these aFSs are in series. Accordingly, the energy densities of G-CNO and M-CNO reach 4.01 and 2.39 mWh/cm^2 (or 238.7 and 188.3 mWh/cm^3) at the outstanding power densities of 28.0 and 28.2 mWh/cm^2 (or 1.97 and 2.2 W/cm^3), respectively.

These results demonstrate that the hybrid FS can deliver a high power density without substantially losing its stored energy. To compare the electrochemical properties of the prepared FSs with those of similar systems reported in the literature, an example radar plot is constructed as shown in Fig. 4g. Notably, a large area in the radar plot indicates a superior overall performance. The G-CNO and M-CNO aFSs synthesized in this study display large coverage areas in the radar plot, and these large areas confirm their remarkable electrochemical performances, high specific capacitances, high energy densities, and wide potential windows. The data presented in Table S2 and Fig. 4g indicate that the G-CNO and M-CNO aFSs outperform all the previously reported high-performing aFSs. Moreover, the CNO sFS also exhibits a remarkably high energy density and a considerably large area in the radar plot, which suggests that its electrochemical potential is comparable to, or even superior to, those of various other previously reported FSs (Table S1). Moreover,
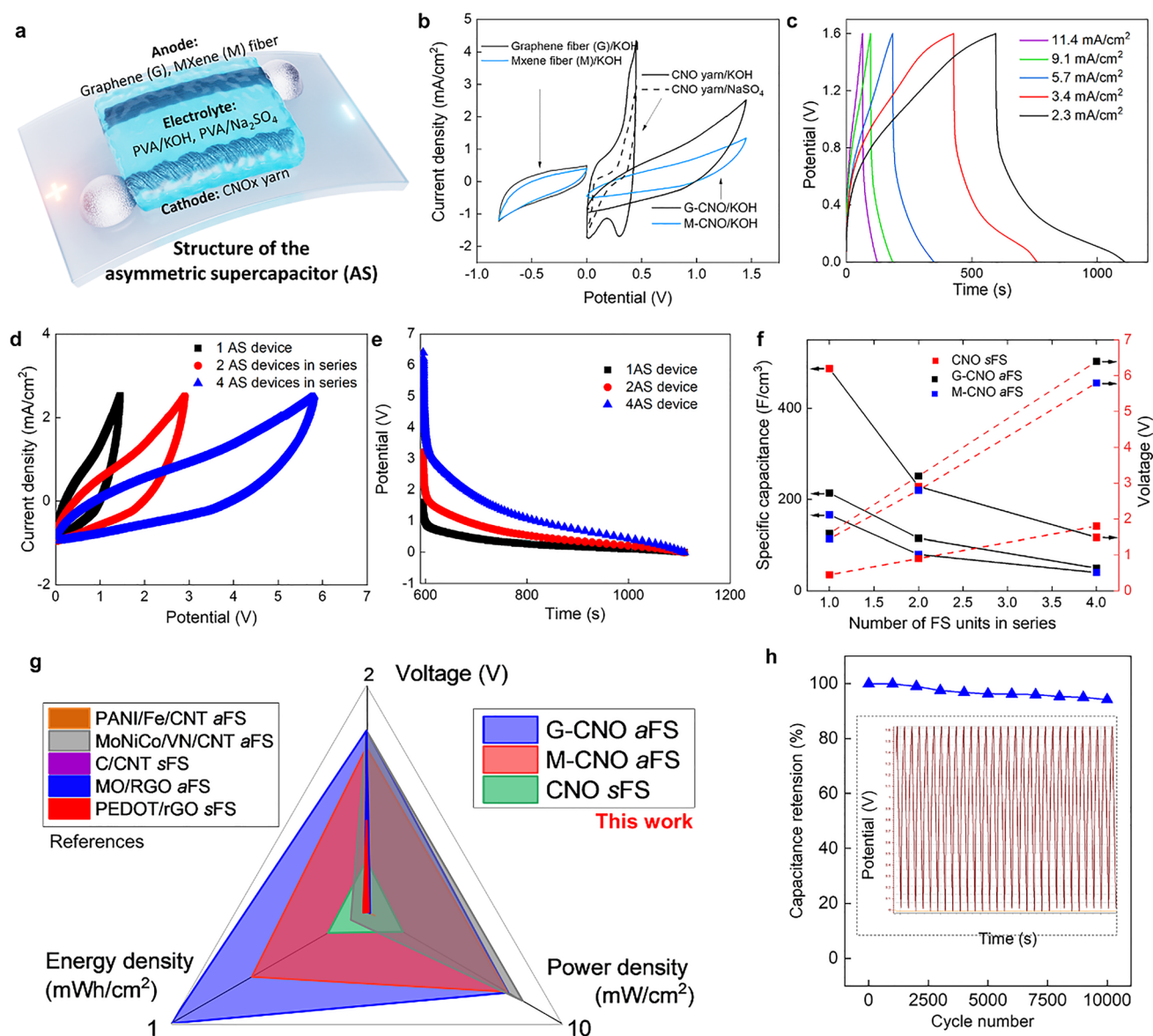
Fig. 4 Electrochemical performances of the aFSs. **a** Schematic representation of the aFS structure. **b** CV plots and corresponding voltage windows of the GF, MF, and CNO yarns. **c** GCD plots recorded at various current densities for the G-CNO aFS. **d** CV and I GCD plots for the G-CNO aFS when connected in series. **f** Variation in the specific capacitance (solid black-colored line) and voltage window (bro-ken red-colored lines) upon changing the number of units connected in series. **g** Radar plot comparing the electrochemical performances of the FSs with those of previously reported systems. **h** Capacitance retention performance of G-CNO aFS and its corresponding GCD profile during the final 30 test cycles

analysis of the cycling stability of the G-CNO aFS revealed an impressive 94.2% retention of the initial capacitance after 10000 cycles (see Fig. 4h). These findings establish the prepared G-CNO aFS as a highly promising candidate for developing advanced energy storage materials.

2.3 Flexibility of the CNO Nanoribbon Yarns

To confirm that the CNO yarn-based FSs can be applied and integrated with flexible and wearable electronic

devices in practical applications, a bending test was conducted to determine the effects of bending on the electrical resistance of the prepared FSs. Figure 5a indicates that the resistance changes in the range of 0–0.9% at a curvature of 5.21 cm^{-1}. A more rigorous evaluation involving 1000 bending cycles verifies the structural stability of the yarn, highlighting its ability to maintain consistent electrical contact within the nanoribbon network despite being subjected to repeated mechanical stresses. Throughout these 1000 bending cycles, the nanoribbon yarn consistently
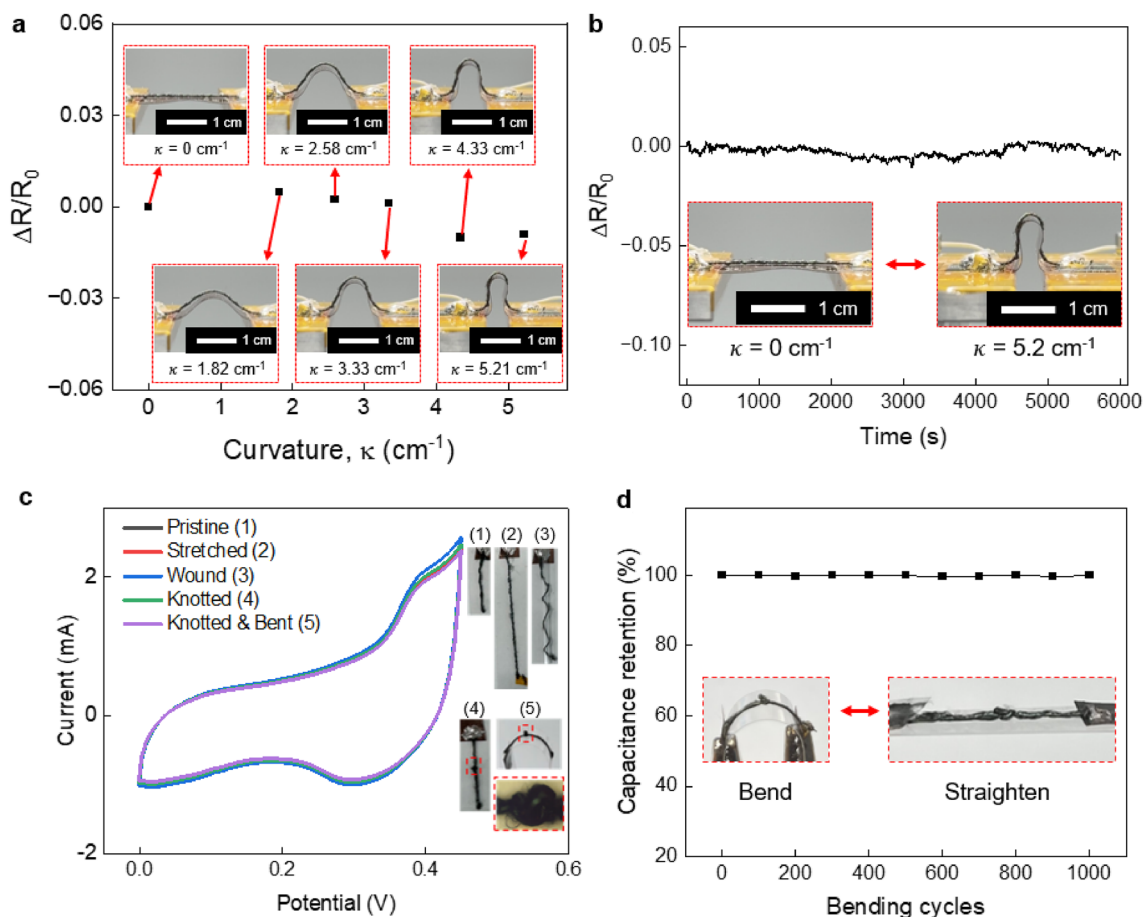
Fig. 5 Effects of bending on the electrical and electrochemical responses of the CNT nanoribbon yarn. **a** Results of the bending test performed on the CNO nanoribbon yarn for curvatures up to ~ 5.21 cm^{-1}. **b** Results of cyclic bending tests performed at a curvature of 5.21 cm^{-1} over 1000 cycles. **c** CV plots and corresponding optical images of the CNO yarn FS following the application of various mechanical deformation conditions. **d** Capacitance retention of the CNO yarn FS after different bending cycles. The corresponding optical images are shown in the inset

exhibits a stable electrical resistance with < 1.00% variations (Fig. 5b).

Furthermore, the CV profiles of the CNO FS that underwent mechanical deformation, including stretching, winding, knotting, and bending after knotting were measured. Notably, Fig. 5c reveals that the CV profiles of these mechanically deformed FS samples are almost identical to those of the pristine FS. The capacitance retention of the CNO sFS was assessed by measuring its GCD profile at a current density of 69.4 mA/cm^3 during 1000 repeated bending (90°) and straightening (180°) cycles. Figures 5d and S10 indicate that the CNO sFS maintains a specific capacity of (493 ± 1.05) F/cm^3, which reaffirms the ability of this device to maintain its excellent performance during mechanical deformation. Therefore, these results indicate that the developed CNO FS exhibits a high strain-independent electrical resistance and consistent capacitance retention, and is thus suitable for integration into wearable energy storage devices.

2.4 Application of the FS as an Energy Storage Component in Smart Textiles

The potential of the developed aFS for application as an energy storage component in smart textiles was demonstrated by integrating it with various electronic devices, including an energy harvester, a pressure sensor, and a flexible LED (Fig. 6a). Initially, to charge the aFS, a single-electrode TENG was developed using a Au nanoribbon yarn. The TENG system was designed to integrate a single layer Au nanoribbon yarn (as a positive component) directly onto a polypropylene melt-blown mask (as the negative component) (Fig. 6b). The fabricated TENG effectively converted the mechanical energy generated during human inhalation and exhalation into electrical energy by leveraging the contact and separation motion of the nanoribbon yarn with the mask (see Fig. S11a). During breathing from mount, the Au nanoribbon yarn exhibited mechanical vibrations, leading to the generation of a maximum peak-to-peak voltage of 46 V
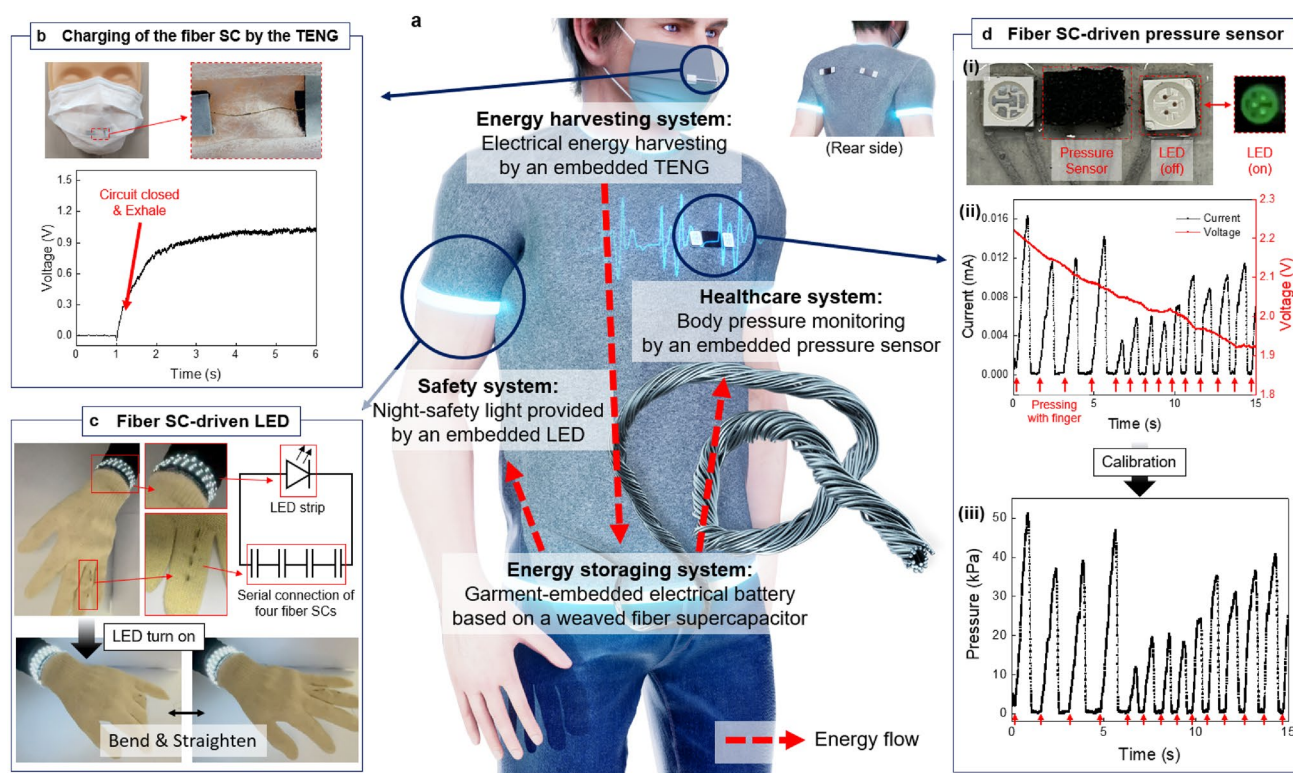
Fig. 6 Application of the aFS as an energy storage component in smart textiles. **a** A comprehensive wearable electronic system integrating harvesting, storage, and powering functionalities, demonstrating the future of smart textiles. In this system, a TENG is used to charge the aFS, which subsequently powers the pressure sensor and the flexible LEDs. **b** Photograph showing the TENG integrated into a mask. The experimental results obtained for the harvesting of mechanical energy from human breathing and its storage in the aFS

are also presented. **c** Photograph showing the aFS integrated into the commercialized glove and subsequent powering of a flexible LED in bent and straightened states. **d-i** Photograph showing a multifunctional wearable device based on a pressure sensor and an LED. **d-ii** Current and voltage outputs of the pressure sensor powered by the aFS under repeated mechanical pressing by a finger, and **d-iii** its data calibrated according to the applied pressure

(see Fig. S11b). By connecting the fabricated TENG to the aFS using a circuit containing a rectifier (i.e., to convert the negative voltage output into a positive voltage, see Fig. S11a), the supercapacitor was successfully charged using the energy harvested from the motions involved in the breathing process of humans. This process resulted in a voltage increment of up to 1 V within 5 s for the aFS (Figs. 6b, S11c, and S11d). Notably, this demonstration highlights the promising compatibility of the developed FS with a general TENG as well as the versatility of the proposed nanoribbon yarn forming process for fabricating various electronic devices. This proposed method opens new avenues for integrating these nanoribbon yarns and utilizing them in a broad range of electronic devices (such as energy harvesters, physical and chemical sensors, and energy convertors), ultimately expanding the application scope of this technology to smart textiles and wearable electronics.

Subsequently, the aFSs were connected in series to light a commercial flexible LED lamp (driving voltage, 1.5–2 V; shown in Fig. 6c). Four fully charged aFSs (each 1.5 cm in

length) connected in series aided the operation of the LED array for approximately 25 s (Fig. S12). The excellent electrochemical properties exhibited by this series were mainly attributed to the synergetic combination of the superior charge transfer kinetics offered by the electrically conductive GF and the porous structure (see Supplementary Note 1) of the battery-like CNO fiber (Fig. S5), which facilitated ionic and electron transfer and suppressed volumetric changes in the electrode during the charge–discharge process. These results demonstrate the potential of this system for use as an efficient power source with excellent stability. The sustainability of the achieved LED lighting was also tested under repeated bending/releasing cycles (Movie S1). The obtained results indicate that such devices can be integrated into our daily clothes as wearable power sources owing to their compatibility with human motion.

Finally, a complex wearable electronic device was assembled, consisting of a piezoresistive pressure sensor array with integrated LEDs, similar to the one reported in our previous study (Figs. 6d-i and S13) [50]. Each pressure

sensor in the array was composed of a porous elastomer and CNT composite. Upon the application of pressure to the sensor, the inner CNTs established contact with each other, and consequently, the electrical resistance decreased. To demonstrate the feasibility of powering the sensor using the developed FS and to determine the change in the electrical resistance of the sensor, the aFS was connected to a single pressure sensor, and random pressure was applied by a finger. During the discharge of the FS by the connected pressure sensor, the current in the series circuit and the voltage of the pressure sensor were monitored (Fig. S13a). While the overall current and voltage gradually decreased during the discharge, the current signal varied with the applied pressure, reflecting the resistance change of the pressure sensor (see Figs. 6d-ii and S13b). The applied pressure was subsequently calculated using calibration plots (Figs. 6d-iii and S13c). In addition, similar to the results obtained in the abovementioned LED experiment, the integrated LED was turned on by the charged aFS (Fig. 6d-i); this observation confirmed the compatibility of the aFS with complex devices. The overall energy balance of energy harvesting, storage, and consumption is described in Supplementary Note 2. Although each device was individually driven to demonstrate its feasibility in real-life applications, the compatibility of the developed aFS with complex wearable electronics was successfully demonstrated.

Overall, this demonstration suggests that integrating multiple aFSs in parallel within a fabric is conducive to rapid charging through wearable TENGs while powering multiple conventional wearable devices. Such an integrated system holds significant promise application as a supercapacitor, whose charge and discharge cycles are faster than those of conventional batteries. Thus, the proposed FSs can be employed as key devices for enhancing the performances and functionalities of next-generation wearable electronics and smart textiles.

3 Conclusions

In this study, a new fabrication approach was devised to produce high-performance FSs using physically deposited TMO nanoribbon yarns. Through the precise control of interface adhesion, dimension-controlled nanoribbon yarns composed of NiO_x, MnO_x, and $CoNi_xO_y$ were successfully prepared. These nanoribbon yarn FSs exhibited excellent electrochemical activities and long-term stabilities. Additionally, an aFS device, which combined GFs with a CNO yarn, demonstrated remarkably high energy and power densities. Furthermore, the nanoribbon yarn FS was successfully integrated into a comprehensive wearable electronic system, encompassing energy harvesting, energy storage, and powering sensing/display devices. In this system, a TENG

was used to charge the FS, and thus, it can be employed to power wearable pressure sensors and flexible LEDs. Despite the significant progress achieved in the field of energy storage materials, challenges pertaining to the physical deposition method still exist, and one of these challenges involves controlling the stoichiometry of TMOs; specifically, the e-beam evaporation process used for TMO deposition can result in stoichiometric changes due to the different vaporization points of individual chemical elements. To address this issue, employing a sputtering process, wherein the stoichiometry remains relatively constant during deposition, offers a potential solution. The proposed approach is expected to facilitate precise control of the physical dimensions of FSs as well rational engineering of their chemical compositions. Moreover, the identification of energy storage materials that are suitable for the emerging next-generation electrochemical energy storage devices, based on nanoscale composite electrodes, has become challenging. For instance, nanoscale porous materials significantly reduce the number of ionic diffusion pathways in a battery such that ionic diffusion becomes negligible. Thus, research on energy storage materials is gradually transitioning toward primarily surface-based electrochemical processes such as those applied in the synthesis of pseudocapacitors. Size effects, combined with surface and interfacial phenomena, expedite the redox kinetics, and thus, differentiating between battery and pseudocapacitive materials solely based on kinetic analyses has become challenging. However, this study represents a significant advancement in hybrid TMO-based FS technologies, and the fabricated FSs achieve the highest capacitance and energy density reported to date. It also marks the first demonstration of comprehensive wearable electronic systems integrated with energy harvesting, storage, and powering functionalities. The ability to fabricate physically evaporated TMO yarns with a high precision also paves the way for the development of a high-performance FSs with enhanced stability and outstanding electrochemical performances. Furthermore, it opens up new possibilities for customizing FSs to suit specific applications in wearable electronics and energy storage systems. Overall, our study findings provide valuable insights and a conceptual roadmap for the development and integration of FSs across various industries, including smart textiles, wearable health monitoring, portable electronics, and the Internet of Things, in the future.

4 Methods

4.1 Fabrication of the Trilayer Nanoribbon Yarns

A Si master nanoline mold (width: 800 nm, pitch: 1600 nm, depth: 2000 nm) was fabricated using krypton fluoride lithography. The mold was then replicated by pouring

RM-311 polyurethane resin (Minuta Technology Co., Ltd., Korea) into the mold and covering it with an ultraviolet (UV)-transparent PET film. To ensure proper penetration of the resin into the nanopattern, a controlled pressure was applied using a customized roller. Subsequently, the resin was cured under UV light and separated from the Si master mold [51–57]. The target materials (TMO/metal/TMO trilayers) were then sequentially deposited onto the replicated nanoline mold using e-beam evaporation (Daeki Hi-Tech Co., Ltd., Korea), and the polymeric nanoline mold (bearing the deposited materials) was subjected to selective etching via oxygen plasma treatment (plasma power = 100 W, flow rate = 50 sccm). After 2 h of etching, the polymer nanoline mold was sufficiently undercut, resulting in the suspension of the deposited materials in a nanoribbon array form [58]. The suspended nanoribbon array was then delaminated using tweezers and loaded onto a customized yarning machine. After applying a compressive strain of 10%, the nanoribbon array was twisted at a rate of 7 turns per cm to generate the nanoribbon yarn.

4.2 Characterization of the Nanoribbon Yarns

Field-emission TEM combined with EDS (HD-2300A, Hitachi, Japan) was employed to record the cross-sectional images of the polymeric nanoline mold containing the deposited trilayer materials and to determine the material composition of each layer. For side-view imaging at varying plasma treatment times, a dual, focused ionic beam integrated with SEM (Helios NanoLab™, FEI, Netherlands) was employed. Ultra-high-resolution field-emission SEM combined with EDS (SU8230, Hitachi, Japan) was used to verify the surface morphologies and overall material compositions of the resulting nanoribbon yarns. Binding energy analysis for each chemical element present in the nanoribbon yarns was performed using XPS (K-Alpha+, ThermoFisher Scientific, USA).

4.3 Fabrication of the GF

A solution of GO (2 wt%), featuring an average flake size of 100 um, was purchased from Grapheneall (South Korea). A wet spinning process was employed to produce the desired GO fibers; specifically, a 2 wt% aqueous GO solution was spun through a syringe pump into a coagulation solution placed on a rotating disk, wherein the coagulant consisted of 1 wt% dopamine chloride and 0.67 wt% copper nitrate. Subsequently, the spun fibers were washed with water and air-dried for 12 h at ~ 25 °C, before subjecting to thermal reduction for 2 h at 1000 °C (heating rate = 10 °C/min) under a hydrogen atmosphere to obtain the desired GFs.

4.4 Fabrication of the MFs

The $Ti_3C_2T_X$ MXene was synthesized by delaminating the Ti_3AlC_2 MAX phase (average flake size = 40 μm) purchased from Carbon-Ukraine Ltd. (Ukraine); specifically, 12 mol/L HCl was mixed with deionized (DI) water and a 50 wt% HF solution (6:3:1 volumetric ratio) in a 250 mL bottle. Subsequently, the Ti_3AlC_2 MAX phase powder (3 g) was combined with this mixture and stirred at 400 revolutions per minute (rpm) and 35 °C for 24 h. Subsequently, the obtained mixture was purified by centrifugation (3500 rpm at 10 °C) with a large volume of DI water until the pH was in the range of 5–6. A 0.5 M solution of LiCl was then added to the purified product (150 mL) and stirred at 400 rpm and ~ 25 °C for 4 h; this solution was then purified by centrifugation with DI water (500 mL; 3500 rpm at 10 °C for 20 min; 8000 rpm at 10 °C for 30, 45, and 60 min). The resulting $Ti_3C_2T_X$ MXene was collected from the supernatant after centrifugation at 4400 rpm and 5 °C for 1 h.

4.5 Wet Spinning of the $Ti_3C_2T_X$ MF

A 7 wt% $Ti_3C_2T_X$ MXene solution was spun onto a 0.03 mol/L ethylenediamine solution using a syringe pump. The spun fibers were then air-dried and subjected to a two-step reduction process. Specifically, the first step involved chemical reduction using hydriodic acid (Sigma–Aldrich) at 80 °C for 12 h. Second, the resulting fibers were thoroughly cleaned and air-dried, and then annealed at 400 °C for 1 h (heating rate = 10 °C/min) in an Ar atmosphere to achieve the desired MFs.

4.6 Preparation of the PVA/KOH Polymer Gel Electrolyte

PVA (3 g) was dissolved in distilled water (20 mL) under stirring at 90 °C for 2 h. As the solution turned transparent, a KOH solution (0.3 g/mL) was added dropwise under magnetic stirring until a clear, gel-like consistency was achieved.

4.7 Fabrication of the Symmetric/Asymmetric Supercapacitors

All solid-state sFSs were fabricated by assembling two identical TMO yarns (CNO, MO, or NO) of the same lengths and diameters on a flexible PET film or a fabric substrate. These yarns were arranged in a parallel pattern with the help of a double-sided Cu tape to secure one end of each yarn to the substrate. Electrical contact was ensured by coating Ag paste onto this same end. Subsequently, a generous coating of the PVA/KOH polymeric gel was applied to the yarns using a paintbrush, and the assembly was allowed to dry for 30–60 min under vacuum conditions. A similar protocol was

followed for the fabrication of all-solid-state aFSs, with the exception that the TMO yarns (CNO, MO, and NO) were assembled as the positive electrode, and a GF or an MF was used as the negative electrode. Both the positive and negative electrodes were charged and mass-balanced to achieve an optimal electrochemical performance.

4.8 Characterization of the FSs

The CV, GCD, and EIS measurements were performed on an electrochemical workstation (Bio-Logic SAS SP-200 model). The capacitance of each FS (C_s) was calculated from the charge–discharge plots using the following equation [4, 11, 12]:

$$C_s = i/\left(\frac{dV}{dt}\right) \tag{1}$$

where i, dV, and dt represent the discharge current, voltage, and time, respectively. The specific capacitance related to an individual electrode (C_f) was calculated as follows:

$$C_f = 2C_s \tag{2}$$

In addition, the areal ($C_{f,area}$) and volumetric capacitances ($C_{f,volume}$) of the fibers were calculated by dividing C_f by the area and volume of the individual fiber, respectively. SEM was used to determine the lateral sizes of the fibers for the area and volume calculations. The areal ($C_{s,Area}$) and volumetric capacitances ($C_{s,volume}$) of the supercapacitor devices were calculated using the following equations,

$$C_{s,\ area} = C_S/Area_s \tag{3}$$

$$C_{s,\ volume} = C_S/Volume_s \tag{4}$$

where $Area_s$ and $Volume_s$ are the area and volume of the supercapacitor device, respectively, and include contributions from the electrolyte and space between the fibers. The energy densities (E_s) and power densities (P_s) of the supercapacitors were obtained using the following equations:

$$E_{s,volume} = C_{s,volume}\Delta E^2/(2 \times 3600) \tag{5}$$

$$P_{s,volume} = E_{s,volume} \times 3600/t_{discharge} \tag{6}$$

where ΔE is the difference between the operating voltages (V), and $t_{discharge}$ is the discharge time.

4.9 Flexibility Analysis

To conduct the bending tests and evaluate the electrical resistance, the $CoNi_xO_y$ nanoribbon yarn was prepared and attached to a PET film (thickness = 0.1 mm) by applying Ag paste at both ends of the nanoribbon yarn. An external electrical wire was then connected to the nanoribbon yarn. Subsequently, the PET film bearing the nanoribbon yarn was affixed to a custom-made linear stage using carbon tape and was then subjected to compression to induce buckling. During the buckling process, the curvature of the nanoribbon yarn was measured at each step using a camera, while the resistance of the nanoribbon yarn was monitored using a source meter (2400, Keithley, USA). The electrochemical stabilities of the CNO FS were evaluated using a Bio-Logic electrochemical workstation. The repeated bending and stretching cycles for testing the electrochemical stability of CNO sFS were achieved using a homemade automated stretching/bending test device, which was fixed for a 90° bending angle and 180° straightening angle. The CNO sFS prepared on a PET substrate was held by stretching test equipment, with its positive and negative edges clamped by both platinum holders of the stretching equipment and Bio-Logic electrochemical workstation.

4.10 Smart Textile Applications

Three tests were conducted to evaluate the performances of the CNO FS in various applications. In the first test, the CNO FS was charged using a single-electrode TENG system, which was fabricated by integrating an Au nanoribbon yarn directly onto a polypropylene-based melt-blown mask filter. The nanoribbon yarn was attached using carbon tape to which an external electrical wire was connected. The open-circuit voltage between the ground and the electrical wire was measured using an oscilloscope (MDO3022, Tektronics, USA). The CNO FS was also connected to the oscilloscope, and the charged voltage was measured during repeated exhalation and inhalation cycles. In the second test, a piezoresistive wearable pressure sensor integrated with an LED, developed by our research group, was used for demonstration [50]. After fabrication of the pressure sensor, the change in its electrical resistance under an applied pressure was measured using a tensile tester (AG–X, Shimadzu, Japan) and source meter (2400, Keithley, USA) for calibration. The prepared CNO FS was initially charged using a commercial 9 V battery to facilitate repeated experiments. Subsequently, the FS was connected to the prepared pressure sensor by closing the switch of the circuit. During the discharge of the FS by the connected pressure sensor, a random pressure was applied by a finger, and the current and voltage of the pressure sensor were monitored using two electrometers (6514, Tektronix, USA). The electrical resistance of the sensor was then calculated using Ohm's law to determine the applied pressure. In the third test, the prepared CNO FS was initially charged using a commercial 9 V battery. It was then directly connected to the flexible LED for powering purposes.

Declarations

References

1. Kou L, et al. Coaxial wet-spun yarn supercapacitors for high energy density and safe wearable electronics. *Nat Commun*. **2014**;*5*:1–10.
2. Zhang Z. Light-emitting materials for wearable electronics. *Nat Rev Mater*. **2022**;*2022*(7):839–40.
3. The many faces of wearables. Nat Electron. 2022;5:709.
4. Liu L, Yu Y, Yan C, Li K, Zheng Z. Wearable energy-dense and power-dense supercapacitor yarns enabled by scalable graphene-metallic textile composite electrodes. *Nat Commun*. **2015**;*6*:7260.
5. Zheng F, et al. A highly sensitive CRISPR-empowered surface plasmon resonance sensor for diagnosis of inherited diseases with femtomolar-level real-time quantification. *Adv Sci*. **2022**;*9*:2105231.
6. Chen Z, et al. A CRISPR/Cas12a-empowered surface plasmon resonance platform for rapid and specific diagnosis of the Omicron variant of SARS-CoV-2. *Natl Sci Rev*. **2022**;*9*:nwac 104.
7. Xue T, et al. Ultrasensitive detection of miRNA with an antimonene-based surface plasmon resonance sensor. *Nat Commun*. **2019**;*10*:28.
8. Li C, Jia R, Yang Y, Liao G. A hierarchical helical carbon nanotube fiber artificial ligament. *Adv Fiber Mater*. **2023**;*2023*(5):1549–51.
9. Zheng Y, et al. Electrochemical exfoliation and growth of nickel–cobalt layered double hydroxides@black phosphorus hetero-nanostructure textiles for robust foldable supercapacitors. *Adv Funct Mater*. **2024**;2401738
10. Zhu X, et al. Microfluidic-assembled covalent organic frameworks@Ti_3C_2Tx MXene vertical fibers for high-performance electrochemical supercapacitors. *Adv Mater*. **2023**;*35*:2307186.
11. Qu G, et al. A fiber supercapacitor with high energy density based on hollow graphene/conducting polymer fiber electrode. *Adv Mater*. **2016**;*28*:3646–52.
12. Ren J, et al. Twisting carbon nanotube fibers for both wire-shaped micro-supercapacitor and micro-battery. *Adv Mater*. **2013**;*25*:1155–9.
13. Lima N, et al. Carbon threads sweat-based supercapacitors for electronic textiles. *Sci Rep*. **2020**;*10*:1–9.
14. Choi C, et al. Stretchable, weavable coiled carbon nanotube/MnO_2/polymer fiber solid-state supercapacitors. *Sci Rep*. **2015**;*5*:1–6.
15. Zhai S, Chen Y. Graphene-based fiber supercapacitors. *Acc Mater Res*. **2022**;*3*:922–34.
16. Yu D, et al. Scalable synthesis of hierarchically structured carbon nanotube-graphene fibres for capacitive energy storage. *Nat Nanotechnol*. **2014**;*9*:555–62.
17. Lu Z, et al. Carbon nanotube based fiber supercapacitor as wearable energy storage. *Front Mater*. **2019**;*2019*(6):1–14.
18. Guan T, et al. Recent progress of graphene fiber/fabric supercapacitors: From building block architecture, fiber assembly, and fabric construction to wearable applications. *Adv Fiber Mater*. **2023**;*5*:896–927.
19. Lee S, An GH. Interface engineering of carbon fiber-based electrode for wearable energy storage devices. *Adv Fiber Mater*. **2023**;*5*:1749–58.
20. Zhou Y, Guan F, Zhao F, Shen Y, Bao L. High-energy-density graphene hybrid flexible fiber supercapacitors. *Batter Supercaps*. **2023**;*6*:e202200536.
21. Zhu X, et al. Vertical-aligned and ordered-active architecture of heterostructured fibers for high electrochemical capacitance. *Adv Fiber Mater*. **2024**;*6*:312–28.
22. Padmajan SS, et al. Interface-confined high crystalline growth of semiconducting polymers at graphene fibers for high-performance wearable supercapacitors. *ACS Nano*. **2017**;*11*:9424–34.
23. Tian J, Cui N, Chen P, Guo K, Chen X. High-performance wearable supercapacitors based on PANI/N-CNT@CNT fiber with a designed hierarchical core-sheath structure. *J Mater Chem A Mater*. **2021**;*9*:20635–44.
24. Salman A, et al. Tungsten nitride-coated graphene fibers for high-performance wearable supercapacitors. *Nanoscale*. **2020**;*12*:20239–49.
25. Lim L, et al. All-in-one graphene based composite fiber: Toward wearable supercapacitor. *ACS Appl Mater Interfaces*. **2017**;*9*:39576–83.

26. Cai W, et al. Transition metal sulfides grown on graphene fibers for wearable asymmetric supercapacitors with high volumetric capacitance and high energy density. *Sci Rep*. **2016**;*6*:1–9.

27. Yuan S, et al. Recent progress on transition metal oxides as advanced materials for energy conversion and storage. *Energy Storage Mater*. **2021**;*42*:317–69.

28. Teng XL, Sun XT, Guan L, Hu H, Wu MB. Self-supported transition metal oxide electrodes for electrochemical energy storage. *Tungsten*. **2020**;*2*:337–61.

29. Lei Z, et al. Recent advances of layered-transition metal oxides for energy-related applications. *Energy Storage Mater*. **2021**;*36*:514–50.

30. Wei ZY, et al. Progress in ceramic materials and structure design toward advanced thermal barrier coatings. *J Adv Ceram*. **2022**;*11*:985–1068.

31. Delbari SA, et al. Transition metal oxide-based electrode materials for flexible supercapacitors: A review. *J Alloys Compd*. **2021**;*857*:158281.

32. Georgakilas V, et al. Noncovalent functionalization of graphene and graphene oxide for energy materials, biosensing, catalytic, and biomedical applications. *Chem Rev*. **2016**;*116*:5464–519.

33. Ahn J, et al. Nanotransfer-on-things: From rigid to stretchable nanophotonic devices. *ACS Nano*. **2023**;*17*:5935.

34. Ahn J, et al. Nanoscale three-dimensional fabrication based on mechanically guided assembly. *Nat Commun*. **2023**;*14*:833.

35. Liu LY, et al. Synthesis of Co–Ni oxide microflowers as a superior anode for hybrid supercapacitors with ultralong cycle life. *Chin Chem Lett*. **2017**;*28*:206–12.

36. Karaca E, Gökcen D, Pekmez NÖ, Pekmez K. Electrochemical synthesis of PPy composites with nanostructured MnO_x, CoO_x, NiO_x, and FeO_x in acetonitrile for supercapacitor applications. *Electrochim Acta*. **2019**;*305*:502–13.

37. Peng J, Jeffrey SG. A figure of merit for flexibility. *Science*. **2019**;*366*:690–1.

38. Chen YS, et al. Microscopic mechanism for unipolar resistive switching behaviour of nickel oxides. *J Phys D Appl Phys*. **2012**;*45*:065303.

39. Wang M, et al. Efficiently enhancing electrocatalytic activity of α-MnO_2 nanorods/N-doped ketjenblack carbon for oxygen reduction reaction and oxygen evolution reaction using facile regulated hydrothermal treatment. *Catalysts*. **2018**;*8*:138.

40. Li XC, et al. Coherent nanoscale cobalt/cobalt oxide heterostructures embedded in porous carbon for the oxygen reduction reaction. *RSC Adv*. **2018**;*8*:28625–31.

41. Wang R, Wu J. Structure and basic properties of ternary metal oxides and their prospects for application in supercapacitors. In: Metal oxides in supercapacitors. Elsevier Inc.; 2017. p. 99–132.

42. Xie J, et al. Puzzles and confusions in supercapacitor and battery: theory and solutions. *J Power Sour*. **2018**;*401*:213–23.

43. Sahoo S, Kumar R, Joanni E, Singh RK, Shim JJ. Advances in pseudocapacitive and battery-like electrode materials for high performance supercapacitors. *J Mater Chem A Mater*. **2022**;*10*:13190–240.

44. Reddy Inta H, Koppisetti HVSRM, Ghosh S, Roy A, Mahalingam V. Ni3Se4 nanostructure as a battery-type positive electrode for hybrid capacitors. *ChemElectroChem*. **2023**;*10*:1–11.

45. Kushwaha V, Mandal KD, Gupta A, Singh P. Ni0.5Co0.5S nano-chains: a high-performing intercalating pseudocapacitive electrode in asymmetric supercapacitor (ASC) mode for the development of large-scale energy storage devices. *Dalton Trans*. **2024**;*53*:5435–52.

46. Choi C, et al. Improvement of system capacitance via weavable superelastic biscrolled yarn supercapacitors. *Nat Commun*. **2016**;*7*:1–8.

47. Meddings N, et al. Application of electrochemical impedance spectroscopy to commercial Li-ion cells: A review. *J Power Sour*. **2020**;*480*:228742.

48. Pech D, et al. Ultrahigh-power micrometre-sized supercapacitors based on onion-like carbon. *Nat Nanotechnol*. **2010**;*5*:651–4.

49. El-Kady MF, Kaner RB. Scalable fabrication of high-power graphene micro-supercapacitors for flexible and on-chip energy storage. *Nat Commun*. **2013**;*4*:1475.

50. Kim MS, et al. Skin-like omnidirectional stretchable platform with negative Poisson's ratio for wearable strain–pressure simultaneous sensor. *Adv Funct Mater*. **2023**;*33*:1–10.

51. Jung Y, et al. Spherical micro/nano hierarchical structures for energy and water harvesting devices. *Small Methods*. **2022**;*2200248*:1–11.

52. Zhao ZJ, et al. Wafer-scale, highly uniform, and well-arrayed suspended nanostructures for enhancing the performance of electronic devices. *Nanoscale*. **2022**;*14*:1136–43.

53. Jeong Y, et al. Biomimetic, programmable, and part-by-part maneuverable single-body shape-morphing film. *Adv Intell Syst*. **2023**;*5*:1–12.

54. Zhao ZJ, et al. Large-area nanogap-controlled 3D nanoarchitectures fabricated via layer-by-layer nanoimprint. *ACS Nano*. **2021**;*15*:503–14.

55. Zhao ZJ, et al. Shape-controlled and well-arrayed heterogeneous nanostructures via melting point modulation at the nanoscale. *ACS Appl Mater Interfaces*. **2021**;*13*:3358–68.

56. Ahn J, et al. All-recyclable triboelectric nanogenerator for sustainable ocean monitoring systems. *Adv Energy Mater*. **2022**;*2201341*:1–11.

57. Ahn J, et al. Morphology-controllable wrinkled hierarchical structure and its application to superhydrophobic triboelectric nanogenerator. *Nano Energy*. **2021**;*85*:105978.

58. Ahn J, et al. Nanoribbon yarn with versatile inorganic materials. Small. 2024. https://doi-org-ssl.oca.korea.ac.kr/10.1002/smll.202311736.